Infrared Physics & Technology 86 (2017) 1–10

Contents lists available at ScienceDirect

Infrared Physics & Technology

journal homepage: www.elsevier.com/locate/infrared

Determination of thermal wave reflection coefficient to better estimate defect depth using pulsed thermography

Adisorn Sirikham [a], Yifan Zhao [a,*], Jörn Mehnen [b]

[a] Through-life Engineering Services Institute, Cranfield University, Cranfield MK43 0AL, UK
[b] Design, Manufacture and Engineering Management, University of Strathclyde, G1 1XJ, UK

HIGHLIGHTS

- The thermal wave reflection coefficient can be estimated directly from observed data.
- The reliability of defect depth measurement is improved.
- The sensitivity to noise level and the selection of sampled segment is reduced.

ARTICLE INFO

Article history:
Received 26 June 2017
Revised 11 August 2017
Accepted 16 August 2017
Available online 22 August 2017

Keywords:
Non-destructive testing (NDT)
Least-squares fitting (LSF)
Optimisation
3D heat conduction
Signal-noise-ratio (SNR)
Composite defects

ABSTRACT

Thermography is a promising method for detecting subsurface defects, but accurate measurement of defect depth is still a big challenge because thermographic signals are typically corrupted by imaging noise and affected by 3D heat conduction. Existing methods based on numerical models are susceptible to signal noise and methods based on analytical models require rigorous assumptions that usually cannot be satisfied in practical applications. This paper presents a new method to improve the measurement accuracy of subsurface defect depth through determining the thermal wave reflection coefficient directly from observed data that is usually assumed to be pre-known. This target is achieved through introducing a new heat transfer model that includes multiple physical parameters to better describe the observed thermal behaviour in pulsed thermographic inspection. Numerical simulations are used to evaluate the performance of the proposed method against four selected state-of-the-art methods. Results show that the accuracy of depth measurement has been improved up to 10% when noise level is high and thermal wave reflection coefficients is low. The feasibility of the proposed method in real data is also validated through a case study on characterising flat-bottom holes in carbon fibre reinforced polymer (CFRP) laminates which has a wide application in various sectors of industry.

1. Introduction

Nowadays, non-destructive testing (NDT) is playing a more and more important role to inspect defects/damages of various industrial components. As a highly efficient and powerful NDT technique, Pulsed Thermography is contact free and offers a rapid inspection while covering a large area within a short time frame and thus readily adaptable to in-situ monitoring applications. This technology has been successfully applied to a wide range of areas such as civil engineering [1–3], medicine and biology as well as agriculture [4–9], aerospace [10–15], automotive [16–18] and the manufacturing [19–21] industries.

Quantitative characterisation of defects by extracting shape, size and depth, and estimation of thermal properties have been proven to be effective in Pulsed Thermography [22–30]. Considerable methods have been developed on defect detection and defect depth evaluation. The relationship between the decay of temperature on the inspected surface and time is a widely-used tool to measure defect depth and most of methods are based on frequency domain [31–33] or time domain [34,35]. Many depth measurement methods require a reference point that defines the pre-known sound areas, such as peak contrast time method (PCT) [36,37] and peak slope time method (PST) [35,38]. PCT measures the peak time of the temperature contrast between the considered point and the reference point, and PST detects the peak time of the first derivative of temperature contrast. Both PCT and PST are approximately proportional to the square of the defect depth, whereas the proportionality coefficient of the PCT method depends

* Corresponding author.
E-mail address: yifan.zhao@cranfield.ac.uk (Y. Zhao).

http://dx.doi.org/10.1016/j.infrared.2017.08.012
1350-4495/

on the size of the defect, but the proportionality coefficient of the PST method does not depend on the size of the defect [39]. In general, the reference point is manually chosen from the sound area. Some researchers attempted to obtain the reference point automatically such as Ringermacher et al. [40] and Pilla et al. [41]. The methods without a reference point include logarithm second derivative method (LSD) [42], absolute peak slope time method (APST) [43], lease-squares fitting method (LSF) [44] and nonlinear system identification method (NSI) [45]. In LSD, the temperature decay curve is converted to the logarithm domain, and a polynomial model is then used to fit the curve to reduce temporal noise and save storage space, where the fitting method is called as thermal signal reconstruction (TSR) [42]. The peak of the second derivative of TSR fitting is then used to estimate the defect depth. The APST method multiplies the square root of its time to temperature decay curve and then computes the peak-time of the first derivative of the modified curve, which is used to estimate the defect depth. Similar with APST, the NSI method fits the modified temperature curve using a polynomial model but the difference is that the model order is chosen automatically for each pixel to produce more reliable depth measurement. These methods, including other recently developed fitting methods of thermal data, such as least-square fitting [46] and partial least squares regression [47], can be categorised as parametric methods where the characteristic time for depth estimation is calculated from the fitted model rather than the raw data. A limitation of all these methods is that they are susceptible to noise, typically large in thermography data because the fitted models are data-driven without considering the underlying physics-based models. The LSF method uses a curve fitting technique to fit the temperature decay curve based on a theoretical heat transfer model to determine the defect depth directly. This method is less susceptible to noise but it presumes that the thermal wave reflection coefficient (R) is 1, which is not true for most real situations [39]. Such an assumption can affect the accuracy of the estimated parameters of the heat transfer model using optimisation techniques. It is therefore crucial to estimate the value of R before detecting defect depth or simultaneously. Moreover, the value of R can be used to investigate thermal effusivity of the defect, which has the potential to help quantify the volume of defect or identify the material of defect (e.g., air, water or oil).

Established upon the LSF method, this paper introduces a modified heat transfer model with its fitting method aiming to not only further improve the accuracy of depth measurement but also estimate the thermal wave reflection coefficient from data directly, which has never been achieved before. The proposed method is then validated through analysing numerical simulation data and experimental data on carbon fibre reinforced plastic (CFRP) composites. This paper is organised as follows. The proposed method with related theory background is presented in Section 2. The results and discussions of the numerical simulations and the experimental example are presented in Section 3 while the conclusions are given in Section 4.

2. Methods

2.1. Principle of active thermography

In the pulsed thermographic inspection, a typical experimental setup of which is illustrated in Fig. 1(a), a short and high energy light pulse is projected onto the sample surface through one or two flash lamps. Heat conduction then takes place from the heated surface to the interior of the sample, leading to a continuous decrease of the surface temperature [26] (see Fig. 1(b)). An infrared camera controlled by a PC captures the time-dependent response of the sample surface temperature. If the sample is defect-free, the time when the temperature deviation occurs can be used to estimate the thickness (if thermal diffusivity is known) or thermal diffusivity of local materials (if the thickness is known). For example, as shown in Fig. 1(b), if the thermal diffusivity is known, the thickness of the point 1 and 2 on the inspected surface can be estimated based on the time of temperature deviation, t_1 and t_2 respectively. This approach can be extended to measure defect depth by considering the first time of temperature deviation. The surface temperature due to the back-wall at depth L for a homogeneous plate is given by [48]

$$T(0,t) = \frac{Q}{\sqrt{\pi\rho ckt}}\left[1 + 2\sum_{n=1}^{\infty} R^n \exp\left(-\frac{n^2L^2}{\alpha t}\right)\right] \tag{1}$$

where $T(0,t)$ is the temperature variation of the surface at time t, Q is the pulse energy, ρ is the material density, c is the heat capacity, k is the thermal conductivity of the material, R is the thermal reflection coefficient of the interface with air, and α is the thermal diffusivity.

2.2. The New Least-Squares Fitting method (NLSF)

Sun [44] introduced a least-square fitting (LSF) method for the pulsed thermography using a speculative heat transfer model. This theoretical model is roughly applicable for the time period $0 < t < t_b$, expressed as

$$T(t) \approx \frac{B}{\sqrt{t}}\left[1 + 2\sum_{n=1}^{\infty} \exp\left(-\frac{n^2L^2}{\alpha t}\right)\right] - st \tag{2}$$

where L is the uniform thickness of the sample or the measured defect depth of the sample, α is thermal diffusivity, t is time of the measurement and B is a numerical value. As illustrated in Fig. 2, TA represents the temperature decrease before 3D heat conduction. The slope s is established by linear fitting of the temperature decrease in the time period $t_a < t < t_b$, expressed as T1, where heat transfer takes place through and around the defect. Note s is typically small and zero for a defect-free plate of uniform thickness. The time instants t_a and t_b were optimised and selected as

$$t_a = \frac{L^2}{2\alpha}, \quad t_b = 3t_a \tag{3}$$

The least square fitting method is then used to estimate the other two unknown parameters B and $\frac{L^2}{\alpha}$.

One limitation of this method is that the value of R in Eq. (1) is assumed to be 1, which is true when the thickness of defect (e.g. air gap) is infinite. However, for most of real applications (e.g. detecting delamination of composite), the thickness of defect is very limited and the value of R can be significantly smaller than 1. For such cases, the accuracy of the estimated defect depth is therefore compromised if R is assumed to be 1. Another limitation is that the estimation of s can be difficult due to the challenge to determine the values of t_a and t_b, unless both L and α are pre-known.

To address the above limitations, this paper introduces a modified analytical model aiming to not only estimate the depth more accurately but also measure the thermal wave reflection coefficient. The proposed analytical model is written as

$$\tilde{T}(t,B,W,R,t_s,s) = \frac{B}{\sqrt{t+t_s}}\left[1 + 2\sum_{n=1}^{M} R^n \exp\left(-\frac{n^2W}{t+t_s}\right)\right] - s(t+t_s) \tag{4}$$

where $B = \frac{Q}{\sqrt{\pi\rho ck}}$, $W = \frac{L^2}{\alpha}$, t_s is the starting time of sampling, and M is a large iteration number. The introduction of t_s is unique and it allows the proposed method applicable to any segment of collected data. There are five parameters to be estimated including t_s, R, W, B

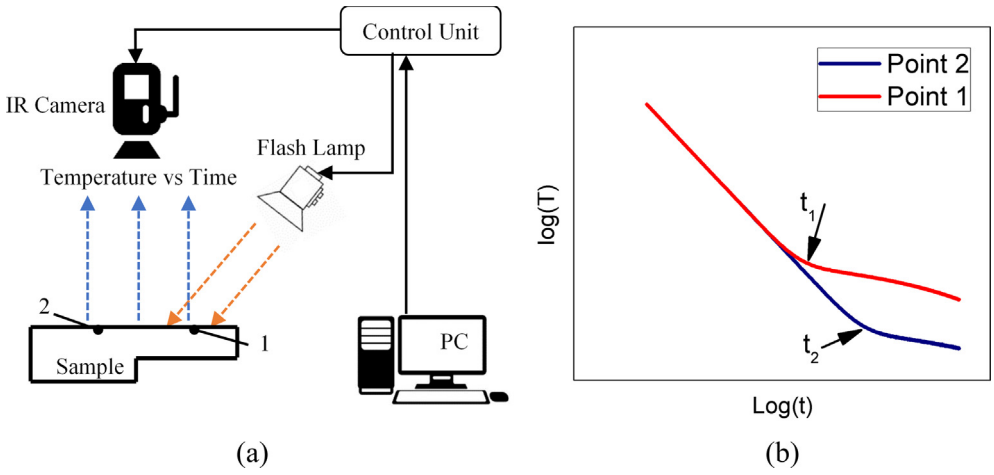

Fig. 1. (a) Experimental configuration of the pulsed thermographic inspection under the reflection mode, where point 1 denotes a location on the sample surface with a thin thickness and point 2 denotes a location with a thick thickness; (b) Typical observed time-temperature decay curves in the logarithmic domain for the point 1 and 2, respectively, where the time of t_1 and t_2 is the key to measure the thickness of local materials [45].

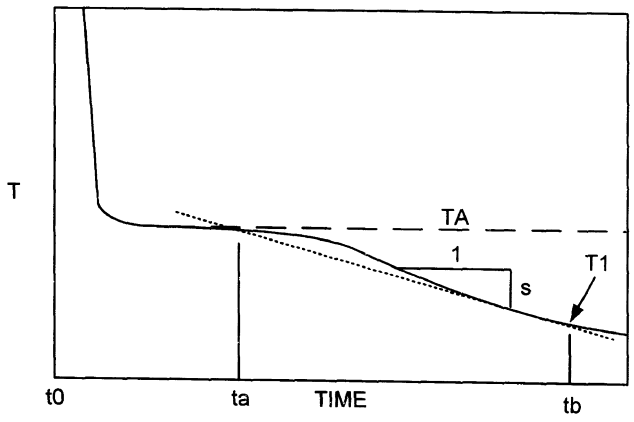

Fig. 2. Surface temperature decay curves [44].

and *s*. This paper employs a nonlinear least-squares solver in Matlab (*lsqnonlin*) to solve this five-parameters optimisation problem. Through initially setting the lower and upper bounds for each parameter, the proposed New Least-Squares Fitting method (NLSF) estimates the optimal parameters that has

$$\min_{B,WR,t_s,s} \|\tilde{T}(t) - T(t)\| \tag{5}$$

The initial value of the parameter t_s is selected as zero and the lower and upper bounds are selected as -1 and 1 respectively because it is usually very small. The initial value of R is selected as 1 and the lower and upper bounds are selected as 0 and 1. The selection of B depends on the energy applied on the inspection surface, and the selection of W depends on the material and thickness of samples (estimated by $W = \frac{L^2}{\alpha}$). The lower and upper bounds of W and A are usually selected as 5 times lower and 5 times higher than the initial values. The lower and upper bounds of s are selected as -50 and 50, and the initial value is chosen as 0. It should be noted that the computational time of this method depends on the selection of initial value and lower and upper bounds.

Once the optimal parameters are estimated, if α is known, the thickness can be estimated by

$$L = \sqrt{W \cdot \alpha} \tag{6}$$

Alternatively, if L is known, the thermal diffusivity can be estimated by

$$\alpha = L^2 \cdot W \tag{7}$$

The temperature contrast ΔT between a defect region and a sound region is dependent not only on the difference between the defect depth and the sample thickness, but also on the lateral size of the defect because of induced 3D heat conduction around the defect. Most of the existing methods, such as PST, LSD, NSI, and APST, tried to estimate the defect depth as early as possible before the 3D heat conduction takes place. These methods work well when the size of defect is large but the accuracy is reduced when the defect size is small due to severe 3D heat conduction, as the results shown in Sun's paper [26]. The proposed equation introduces two extra parameters R and s that consider part of the 3D conduction effect. It can also incorporate the duration effect by introducing the parameter t_s. Therefore, this method can perform better when the 3D conduction and the flash duration effects are present in the flash thermography data.

3. Results and discussions

3.1. Numerical simulations

The aim of these numerical simulations is to compare the performance of the proposed NLSF method with other existing methods against different values of R and noise levels. The time-temperature curves were produced by

$$T(t) = \frac{Q}{e\sqrt{\pi t}}\left[1 + 2\sum_{n=1}^{\infty} R^n \exp\left(-\frac{n^2 L^2}{\alpha t}\right)\right] + \varepsilon(t) \tag{8}$$

and the temperature contrast between defective areas and sound areas by time was simulated by

$$\Delta T(t) = 2\frac{Q}{e\sqrt{\pi t}}\left[\sum_{n=1}^{\infty} R^n \exp\left(-\frac{n^2 L^2}{\alpha t}\right)\right] + \varepsilon(t) \tag{9}$$

where the parameters Q and e were set to 1, α was set to 4×10^{-6} m^2/s, L was set to 4×10^{-3} m and R was varied from 0.1 to 1. The latency of data acquisition was set as zero. The symbol, $\varepsilon(t)$, denotes a white noise sequence with a zero mean and a standard deviation of σ_ε. If σ_T denotes the standard deviation of a signal

without noise, the signal-to-noise ratio (SNR), representing the level of noise, is written as

$$SNR = 20\log_{10}\frac{\sigma_T}{\sigma_\varepsilon} \quad (10)$$

Fig. 3 shows the plots of temperature decay in the logarithmic domain with different values of R. It can be clearly observed that the time of temperature deviation, representing the depth, is independent to the value of R. Furthermore, the value of R determines the slope of the curve after the temperature deviation. If R is 1, the slope is zero, which indicates 100% thermal wave i s reflected by the defect or backwall. If R is zero, there is no temperature deviation occurred.

In the first test, the value of R was set as 1, 0.9, 0.7 and 0.5 respectively, and the noise level was set as 'no noise', 45 dB, 35 dB and 25 dB respectively. The sample rate was set as 50 Hz and totally 250 data points (5 s) were sampled. The LSD, APST, LSF and NLSF methods were applied on the data produced from Eq. (8), while the PST method (temperature contrast based) was applied on the data from Eq. (9). The produced data for PST, LSD and APST methods were fitted by a polynomial model (8th order). For the LSF and NLSF methods, the bounds of optimisation parameters were set as: $0 \le B \le 2000$, $0 \le W \le 50$, $-50 \le s \le 50$; for the NLSF method, two extras parameters are added with the bounds of $0 \le R \le 1$ and $-1 \le t_s \le 1$. Assuming that the value of α is preknown, the mean and standard deviation of depth measurement are summarised in Table 1. The key plots of the compared methods, including the characterise time of PST, LST and APST, and the model fitting of LSF and NLSF, are shown in Table 2.

Under a perfect condition, where there is no noise and R equals to 1, as shown in Table 1, the measured thickness of PST, LSD and APST methods is about 4.06–4.07 mm, within 1.5% percentage error of the ground truth (4.00 mm), and the LSF and NLSF methods produced perfect results (4.00 mm). When R decreases from 1 to 0.5, the measurement error of LSD increases to 0.22 mm (5.5% percentage error), whereas the PST and APST methods produced relatively good and consistent results. The error of estimated thickness of LSF increases slightly (up to 2% percentage error) following the decrease of R. The NLSF method still produced the perfect results for all four R values. Summarily, this test demonstrates that in the case of noise free, the PST, APST, and LSF methods are less sensitive to R, whereas the LSD method is more sensitive to R. The NLSF method is not sensitive to the value of R because the proposed mode considers R as a parameter, estimation of which is a by-product of this method.

In practice, raw data are contaminated with noise and other signal degradations [34,49]. Errors of temperature measurement with the infrared camera are typically classified into errors of the method, errors of the calibration, and errors of the electronic path [50]. The performance of all five considered methods was analysed and evaluated by adding white Gaussian noise to the simulated signal. Three levels of noise were considered: low level of noise (45 dB), medium level of noise (35 dB), and high level of noise (25 dB). For each considered noise level, 1000 tests were repeated and the mean and standard variation of the estimated thickness was computed. The mean indicates the accuracy of measurement, and the standard deviation (std) indicates the precision of measurement. It can be observed from Table 1 that at the low level of noise (45 dB), the mean of measurement of each method is similar as those of no noise. The LSF and NLSF methods produced a high precision (std: 0.01–0.02 mm) than the other three methods (std: 0.07–0.12 mm) when $R = 0.5$. Considering both accuracy and precision, the proposed NLSF performs best. At the medium level of noise (35 dB), the accuracy of the PST, LSF, and NLSF methods is relatively high (<3%) and consistent, while the accuracy of the LSD and APST method is relatively low (<7.5%) and more sensitive to the change of R. The NLSF method has the best accuracy and the LSF method has the best precision. At the high level of noise (25 dB), the accuracy of the PST is significantly reduced (<8.5%) and the APST method produced the largest error (<22%). The NLSF method still has the best accuracy and almost the same level of precision as LSF. All these observations demonstrate the superior performance of the proposed method against noise.

To further evaluate the performance of LSF and NLSF, Table 3 shows the results for data with very high noise level and very low R value, where the value of R changes from 0.4 to 0.1, and SNR changes from 20 dB to −10 dB. In the case of no noise, it is inferred that the estimated thickness using LSF is strongly dependent on the value of R. The error is increased from 3% to 8% when R is changed from 0.4 to 0.1. However, the results produced by the proposed NLSF method are all perfect. An example of curve fittings using the NLSF and LSF methods is illustrated by Fig. 4 where R is chosen as 0.1 and noise level is 40 dB. Inspection shows that NLSF offers better fitting than LSF due to the introduction of the extra parameters. When noise level is increased from 20 dB to −10 dB, the accuracy of NLSF is consistently higher than that of LSF, while there is no significant difference of precision between two methods.

Table 4 shows the estimated values of R against different noise levels where R is varied from 1 to 0.1. For the cases without noise, the proposed method can estimate the R value perfectly. With the increasing of noise level, the estimation error increases. For the noise level less than 30 dB, the error of estimation is less than 0.02. Furthermore, the sensitivity of R estimation to noise level is dependent on the value of R. Higher the R value is, less influence from the noise.

Another benefit of the proposed method is the introduction of the parameter t_s, which measures the potential latency of the sampled timestamp of thermal data. This time shift could be caused by the latency of data acquisition or data storage. Similar with the impact of the estimation of R, the estimation of t_s aims to further improve the accuracy of depth measurement. This feature is particularly important for data collected using a slow sampling rate. Considering the sample rate as 50 Hz, the potential latency was in the range from 0 to 0.02 s. To evaluate the influence of the latency on the depth measurement, Table 5 shows the results of estimation using the proposal method with and without estimation of t_s, where the noise level was set as 30 dB and R was set as 0.4. Inspection of the result shows that the proposed method can successfully estimate the value of t_s, which is not achievable for the characteristic time based methods such as PST, APST and LSD due to the neglect of the physical model. The value of L was estimated with an error less than 1%. However, if the parameter t_s is not considered in model (4), the error of L measurement

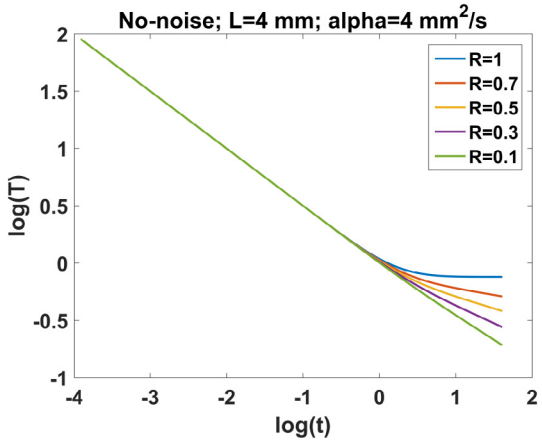

Fig. 3. The comparison of numerical simulation with different values of R, where other parameters are shown on the top of the graph.

Table 1
The comparison of thickness measurement against different noise levels and R values for five selected methods, where the most accurate values are highlighted.

Noise Level	R	Measured Thickness (mm)				
		PST	LSD	APST	LSF	NLSF
No-noise	1	4.06	4.07	4.06	4.00	**4.00**
	0.9	4.06	4.10	4.06	4.01	**4.00**
	0.7	4.06	4.16	4.04	4.04	**4.00**
	0.5	4.06	4.22	4.02	4.08	**4.00**
45 dB	1	4.06 ± 0.04	4.08 ± 0.03	4.06 ± 0.05	4.00 ± 0.01	**4.00 ± 0.01**
	0.9	4.06 ± 0.04	4.10 ± 0.03	4.06 ± 0.06	4.01 ± 0.01	**4.00 ± 0.01**
	0.7	4.06 ± 0.05	4.17 ± 0.05	4.05 ± 0.08	4.03 ± 0.01	**4.00 ± 0.01**
	0.5	4.06 ± 0.07	4.24 ± 0.07	4.05 ± 0.12	4.08 ± 0.01	**4.00 ± 0.02**
35 dB	1	4.07 ± 0.12	4.09 ± 0.08	4.17 ± 0.34	3.99 ± 0.02	**3.99 ± 0.02**
	0.9	4.06 ± 0.13	4.12 ± 0.10	4.19 ± 0.39	4.01 ± 0.03	**4.00 ± 0.03**
	0.7	4.07 ± 0.16	4.19 ± 0.15	4.19 ± 0.42	4.04 ± 0.03	**4.00 ± 0.04**
	0.5	4.08 ± 0.25	4.29 ± 0.24	4.30 ± 0.59	4.09 ± 0.03	**4.01 ± 0.05**
25 dB	1	4.14 ± 0.48	4.14 ± 0.34	4.74 ± 0.82	3.97 ± 0.05	**3.97 ± 0.05**
	0.9	4.13 ± 0.48	4.16 ± 0.37	4.81 ± 0.86	4.01 ± 0.08	**4.00 ± 0.08**
	0.7	4.21 ± 0.74	4.23 ± 0.67	4.87 ± 0.87	4.05 ± 0.10	**4.01 ± 0.12**
	0.5	4.34 ± 1.02	4.17 ± 0.95	4.88 ± 0.89	4.09 ± 0.12	**4.01 ± 0.16**

increases dramatically following the increase of t_s, which suggests the key role of this parameter. It should be noted that in the real applications the ground truth of t_s is unknown. Providing a capability to estimate t_s will increase the reliability of measurement.

Based on above observations, it can be concluded that the proposed NLSF method has significantly improved the robustness and accuracy of depth measurement, particularly when the value of R is significantly lower than 1 or the noise level is high. Meanwhile, the value of R can be effectively estimated. Furthermore, the accuracy of depth measurement of NLSF is immune to the latency of data acquisition while other methods are not.

3.2. Experimental results

A flat plate of carbon fibre reinforced polymer (CFRP) material was used in the second experiment. The size of the composite sample is 153 × 102 × 4 mm. The plate was made of unidirectional Toray 800 carbon fibres pre-impregnated with Hexcel M21 epoxy resin and manufactured in a traditional autoclaving process to a quasi-isotropic layup. Three flat-bottom holes were drilled with the same diameter of 6 mm at different depths (1 mm, 2 mm and 3 mm respectively), as illustrated in Fig. 5. The distance between the holes is 25 mm.

The experiments were conducted with the Thermoscope® II pulsed-active thermography system and comprises of two capacitor bank powered Xenon flash lamps mounted in an internally reflective hood and a desktop PC to capture and store data. The scheme of the experimental set-up is illustrated by Fig. 1(a). A FLIR SC7000 series infrared radiometer operating between 3 and 5.1 μm and a spatial resolution of 640 × 512 pixels was used to perform the inspection. The samples were placed with their surface perpendicular to the camera's line of sight at a distance of 250 mm from the lens. The applied energy was approximately 2 kJ over an inspection area of 250 × 200 mm. Considering the thickness of the sample and its low thermal diffusivity, a sampling rate of 25 Hz was used, and totally 1000 frames, equally 40 s data length, were captured and analysed.

Fig. 6(a) shows a snapshot of the captured thermal image at the time of 8 s, where the middle and bottom holes can be clearly seen. However, the top hole is not detectable in this experiment due to the close distance to the back surface. To further inspect the thermal behaviour, Fig. 6(b) shows the plots of raw temperature curve of three selected pixels over time on the sound area, the middle hole and the bottom hole respectively, the positions of which are marked in Fig. 6(a). The temperature deviation of defective pixels (Point 1 and 2) can be clearly observed at different times while the difference of slope after this deviation is difficult to be distinguished visually. The value of estimated defect depth is dependent on the selection of sampled data, which is a common issue for all depth measurement methods. If the thermal diffusivity and defect depth are known, this selection is straightforward, as suggested by Sun [22]. This paper proposes to use the time when the maximal temperature contrast between the considered defective pixel and the reference pixel from sound area is achieved as the end of sampling. Fig. 6(c) shows the temperature contrast of Point 1 and Point 2, where two peak time t_1 and t_2 are detected. In the proposed method, the data segments of $[0, t_1]$ and $[0, t_2]$ were sampled for the bottom and middle holes respectively. For the sound pixels, the full data length is sampled. To reduce the measurement error of defect depth (L) and thermal wave reflection coefficient (R), ten pixels on the sound region, the middle hole and bottom hole were manually selected and the estimated parameters were averaged. The used thermal diffusivity (α) in this experiment is 0.55×10^{-6} m^2/s. This value was calculated from Eq. (7) on sound area by considering the thickness of the sample as 4 mm.

Both LSF and NLSF methods were applied and the results are shown in Table 6. The averaged estimated depth on the sound area is 3.98 mm and the standard deviation, as an indicator of precision, is 0.04 mm, which is more accurate than those of LSF (3.67±0.05 mm). The measured defect depths of the middle and bottom holes are 2.05 mm and 1.03 mm respectively, which is closer to the ground truth than those of LSF (1.90 mm and 1.06 mm respectively). However, the LSF method produced less standard deviation (0.01 mm and 0.03 mm respectively) than the NLSF method (0.04 mm and 0.06 mm respectively). This observation could be caused by the introduction of two extra parameters. The estimated R value on the sound area is 0.84, which is close to 1, while the s value is 0. The estimated R values for the middle hole and the bottom hole are much smaller (0.18 and 0.25 respectively) and the s values are much larger (0.87 and 16.46 respectively). To further inspect the estimated parameters on difference positions, Fig. 7 plots the scatter of the estimated values of R and s, where ten pixels for each of three regions were sampled. It can be observed that for each region the estimated parameters are relatively consistent while for different regions they are significantly different. Therefore, the clustering of these two parameters can be a potential approach to effectively classify the pixels.

Summarily, the proposed method can estimate both the thickness and defect depth effectively. The error of estimation of the proposed method in the sound area is less than 1% while the LSF

method has error up to 7%. For the defective region, the LSF method produced higher error than the NLSF method around 2%. It should be noted that Eq. (1) is valid only for a homogeneous plate. The composites are non-homogeneous materials. In previous Zhao's work [45], the measured thermal diffusivity of CFRP is about 0.47 ± 0.03 m^2/s, which also depends on the lay-up configuration of the sample. As far as we are concerned, there is no heat diffusion models for non-homogeneous materials, so the assumption that the thermal diffusivity of the tested composite sample is uniform was applied in this paper.

4. Conclusions

This paper has developed a new method that improves the accuracy of defect depth measurement against different levels of noise through estimating the thermal wave reflection coefficient (R) based on the pulsed thermographic inspection. All previous research either neglect the R value or presume that it is pre-known, which increases the uncertainty of depth measurement. This paper firstly provides a solution to estimate the R value directly from observed data. A modified analytical modelling with five parameters is introduced to better fit the observed temperature curve using a nonlinear optimisation technique. The results of the proposed method have been evaluated and compared with four state-of-the-art methods namely PST, LST, APST and LSF based on numerical simulations. The main conclusions of this paper can be summarised as below:

1 Under a noise-free condition: when $R = 1$, the proposed NLSF method and LSF methods produce perfect results for depth measurement while other three methods have errors up to 2%. When the value of R is smaller than 1, the NLSF method

Table 2
The characteristic time of PST, LST and APST, and the model fitting of LSF and NLSF where the blue scatter represents the observations and the red curve represents the fitting.

Noise Level	R	Measured Thickness (mm)				
No Noise	1	PST:(4.06)	LSD:(4.07)	APST:(4.06)	LSF:(4.00)	NLSF:(4.00)
	0.9	PST:(4.06)	LSD:(4.10)	APST:(4.06)	LSF:(4.01)	NLSF:(4.00)
	0.7	PST:(4.06)	LSD:(4.16)	APST:(4.04)	LSF:(4.04)	NLSF:(4.00)
	0.5	PST:(4.06)	LSD:(4.22)	APST:(4.02)	LSF:(4.08)	NLSF:(4.00)
45 dB	1	PST:(4.06±0.04)	LSD:(4.08±0.03)	APST:(4.06±0.05)	LSF:(4.00±0.01)	NLSF:(4.00±0.01)
	0.9	PST:(4.06±0.04)	LSD:(4.10±0.03)	APST:(4.06±0.06)	LSF:(4.01±0.01)	NLSF:(4.00±0.01)
	0.7	PST:(4.06±0.05)	LSD:(4.17±0.05)	APST:(4.05±0.08)	LSF:(4.03±0.01)	NLSF:(4.00±0.01)
	0.5	PST:(4.06±0.07)	LSD:(4.24±0.07)	APST:(4.05±0.12)	LSF:(4.08±0.01)	NLSF:(4.00±0.02)
35 dB	1	PST:(4.07±0.12)	LSD:(4.09±0.08)	APST:(4.17±0.34)	LSF:(3.99±0.02)	NLSF:(3.99±0.02)

(continued on next page)

Table 2 (*continued*)

Noise Level	*R*	Measured Thickness (mm)
	0.9	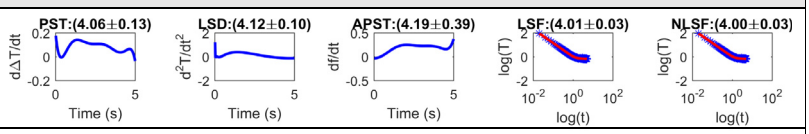
	0.7	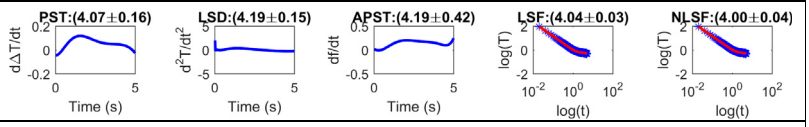
	0.5	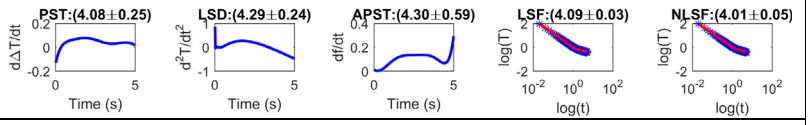
25 dB	1	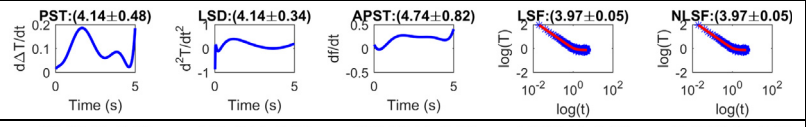
	0.9	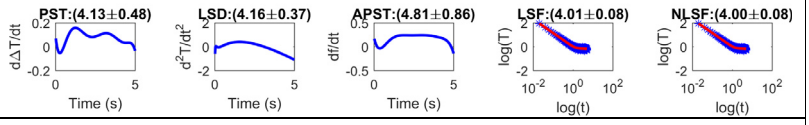
	0.7	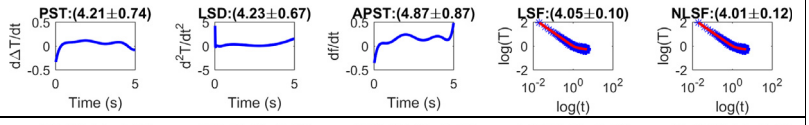
	0.5	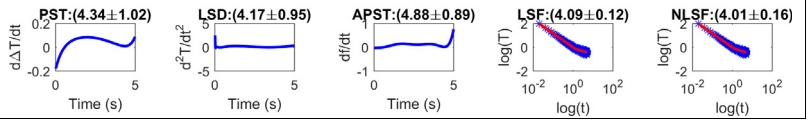

Table 3
The comparison of thickness measurement of the LSF and NLSF methods against high noise level and lower *R* values, where the most accurate values are highlighted.

Noise Level	*R*	Measured Thickness (mm)	
		LSF	NLSF
No-noise	0.4	4.12	**4.00**
	0.3	4.16	**4.00**
	0.2	4.23	**4.00**
	0.1	4.32	**4.00**
20 dB	0.4	4.19 ± 0.33	**4.06 ± 0.32**
	0.3	4.29 ± 0.52	**4.05 ± 0.44**
	0.2	4.55 ± 0.84	**4.10 ± 0.67**
	0.1	5.14 ± 1.42	**4.33 ± 1.21**
10 dB	0.4	4.30 ± 0.73	**4.03 ± 0.85**
	0.3	4.50 ± 0.93	**4.09 ± 1.10**
	0.2	4.74 ± 1.17	**4.25 ± 1.36**
	0.1	5.01 ± 1.56	**4.42 ± 1.79**
0 dB	0.4	4.19 ± 1.14	**4.04 ± 1.50**
	0.3	4.32 ± 1.33	**4.16 ± 1.59**
	0.2	4.36 ± 1.54	**4.26 ± 1.89**
	0.1	4.44 ± 1.56	**4.39 ± 2.00**
−10 dB	0.4	3.59 ± 1.58	**3.94 ± 1.90**
	0.3	3.54 ± 1.59	**3.97 ± 1.94**
	0.2	3.68 ± 1.70	**4.03 ± 1.98**
	0.1	3.64 ± 1.63	**4.16 ± 1.90**

still produces the perfect results while the others four methods produce different levels of imperfect results due to the neglect of *R*.

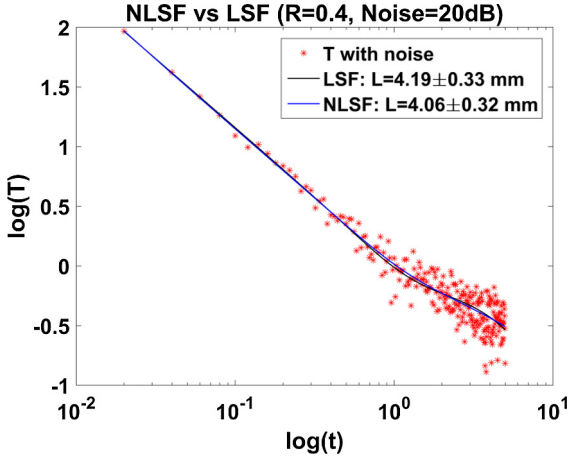

Fig. 4. An example of curve fitting comparison between NLSF and LSF method.

2 Under a noise condition: The observation of measurement accuracy is similar with the noise-free condition. The LSF and NLSF have higher precision of measurement in comparison to PST, LSD and APST. APST has the most sensitivity against noise level and NLSF has the least sensitivity. Such features are important because the signal noise ratio in real applications usually is difficult to be measured and the value of *R* can be different at different places if the material is inhomogeneous.

Table 4
The estimated values of R against different noise levels.

R	Noise Level (dB)							
	No-noise	45	35	25	20	10	0	−10
1	1.00	1.00 ± 0.00	1.00 ± 0.01	0.99 ± 0.02	0.98 ± 0.04	0.95 ± 0.09	0.90 ± 0.19	0.96 ± 0.13
0.9	0.90	0.91 ± 0.01	0.92 ± 0.03	0.94 ± 0.05	0.94 ± 0.07	0.92 ± 0.13	0.92 ± 0.19	0.96 ± 0.14
0.8	0.80	0.81 ± 0.01	0.82 ± 0.03	0.86 ± 0.08	0.87 ± 0.11	0.89 ± 0.16	0.89 ± 0.21	0.96 ± 0.14
0.7	0.70	0.71 ± 0.01	0.72 ± 0.03	0.76 ± 0.09	0.80 ± 0.13	0.85 ± 0.20	0.88 ± 0.23	0.95 ± 0.14
0.6	0.60	0.61 ± 0.01	0.62 ± 0.03	0.67 ± 0.11	0.71 ± 0.15	0.80 ± 0.24	0.86 ± 0.25	0.95 ± 0.14
0.5	0.50	0.51 ± 0.01	0.52 ± 0.03	0.57 ± 0.10	0.63 ± 0.17	0.76 ± 0.27	0.84 ± 0.27	0.96 ± 0.14
0.4	0.40	0.41 ± 0.01	0.42 ± 0.03	0.47 ± 0.11	0.53 ± 0.18	0.70 ± 0.31	0.84 ± 0.27	0.95 ± 0.18
0.3	0.30	0.31 ± 0.01	0.32 ± 0.03	0.37 ± 0.11	0.43 ± 0.18	0.66 ± 0.32	0.86 ± 0.27	0.95 ± 0.17
0.2	0.20	0.21 ± 0.01	0.22 ± 0.03	0.27 ± 0.10	0.36 ± 0.19	0.64 ± 0.35	0.84 ± 0.28	0.95 ± 0.16
0.1	0.10	0.11 ± 0.01	0.12 ± 0.03	0.19 ± 0.12	0.30 ± 0.22	0.63 ± 0.37	0.85 ± 0.28	0.95 ± 0.17

Table 5
Estimated errors of L using the proposed method with and without estimation of t_s, where the noise level was set as 30 dB and the R value was set as 0.4.

True t_s (s)	Including t_s in model (4)					Excluding t_s in model (4)			
	Estimated t_s (s)	L		R		L		R	
		Value (mm)	% Error	Value	% Error	Value (mm)	% Error	Value	% Error
0.019	0.019059	4.0185	0.46	0.4418	10.46	0.0228	99.43	0.9095	127.37
0.017	0.017094	4.0270	0.68	0.4676	16.91	0.1016	97.46	0.6345	58.62
0.015	0.015452	4.0418	1.04	0.5472	36.81	0.1781	95.55	0.4460	11.50
0.013	0.013059	4.0184	0.46	0.4418	10.45	0.2398	94.01	0.3387	15.32
0.011	0.011059	4.0177	0.44	0.4416	10.39	0.3037	92.41	0.2614	34.64
0.009	0.009056	4.0185	0.46	0.4418	10.45	0.3834	90.41	0.2018	49.56
0.007	0.007059	4.0181	0.45	0.4417	10.42	2.3247	41.88	0.2549	36.27
0.005	0.005059	4.0185	0.46	0.4418	10.45	3.0314	24.22	0.3093	22.68
0.003	0.003059	4.0186	0.46	0.4418	10.46	3.4899	12.75	0.3494	12.64
0.001	0.001059	4.0185	0.46	0.4418	10.46	3.8543	3.64	0.3874	3.15

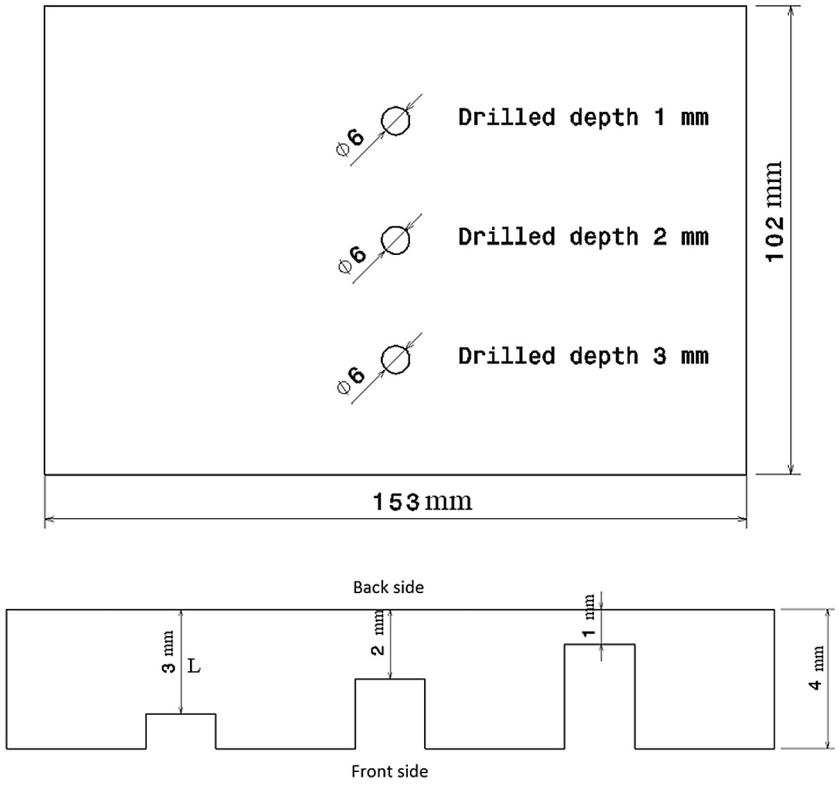

Fig. 5. The composite material sample with drilled in various depth (unit: mm).

3 Due to the introduction of t_s, the proposed method can be applied to any segment of observed data without knowing the start time. Such a feature is attractive for data with a low sampling rate where t_s could be larger than 0 due to accumulated latency by hardware and software of data acquisition. All other four methods neglect the potential variation of t_s, which leads to a guaranteed error, value of which dependents on the value of t_s.

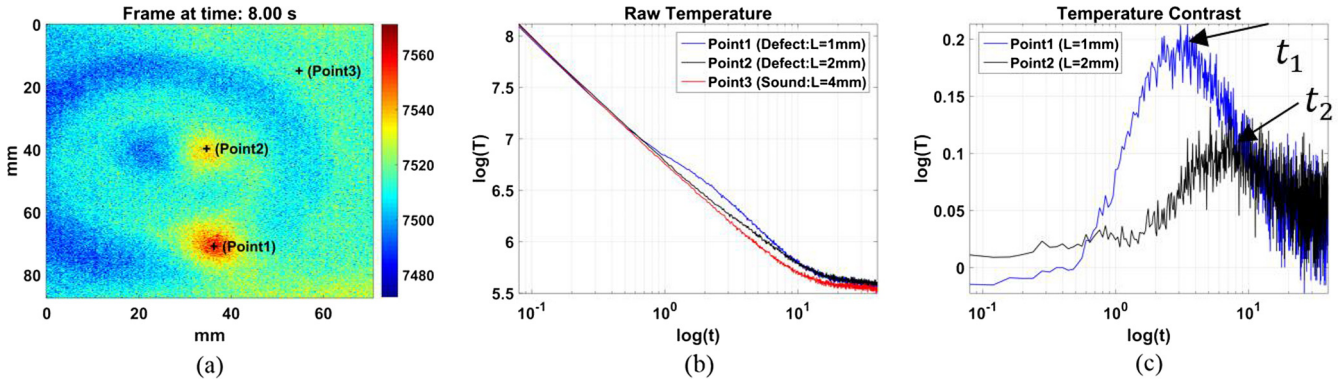

Fig. 6. (a) Raw thermal image at the time of 8 s where three points are sampled from sound area, middle hole and bottom hole respectively; (b) Temperature decay curve of the selected three points in logarithmic domain and (c) Temperature contrast of point 1 and point 2.

Table 6
The measurement of the experimental data using the LSF and NLSF methods.

Position	Ground truth (mm)	Estimated Depth (mm)		Estimated R (NLSF)	Estimated s (NLSF)	Estimated t_s (NLSF)
		LSF	NLSF			
Sound area	4.00	3.67 ± 0.05	3.98 ± 0.04	0.84 ± 0.04	0.00 ± 0.00	0.0226 ± 0.0023
The middle hole	2.00	1.90 ± 0.01	2.05 ± 0.04	0.18 ± 0.02	0.87 ± 0.43	0.0256 ± 0.0011
The bottom hole	1.00	1.06 ± 0.03	1.03 ± 0.06	0.25 ± 0.02	16.46 ± 2.22	0.0269 ± 0.0012

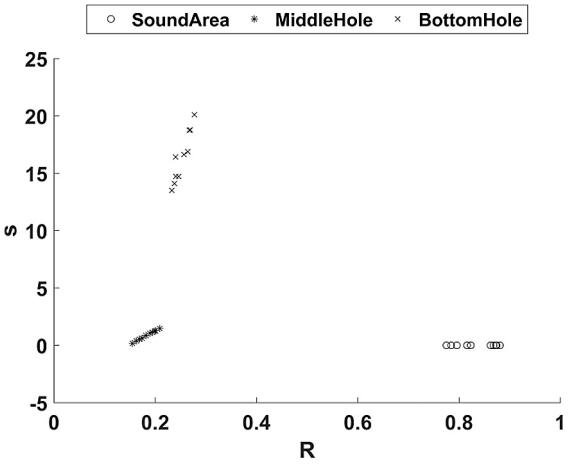

Fig. 7. Scatter chart of the estimated R and s parameters, which shows ten pixels for each of three sampled regions.

4 For the real experimental data, the performance of the proposed method was compared with LSF using the same optimisation technique. Results show that the NLSF method has higher accuracy on defect depth estimation than the LSF method for both defective area and sound area, which suggests an improved reliability of measurement for real data.

One limitation the proposed method is that the accuracy of estimation depends on data length. The depth estimation in sound area needs more data length than defective area. Measurement of deep defect needs more data length than shallow defect. This paper proposes to use the time when maximal temperature contrast between the considered defective pixel and the reference pixel from sound area is achieved to determine the sample length, and the results show that this solution works effectively. The efficiency of this method is affected by the selection of parameters bounds before applying the optimisation technique. Limiting the parameter bounds and setting the initial values closer to ground truth based on result of neighbours could be a solution to reduce the computational time. The proposed method has only been applied to flat bottom holes where a defect has the same depth. This approach has been used for most of other research. If a defect has different depths, the 3D heat conduction is more complex and will have influence on the results. However, due to the consideration of 3D heat conduction by introducing two extra parameters R and s, it is expected that the proposed method will perform even better than other methods though the increased error is inevitable due to the utilisation of 1D heat diffusion model. Performance evaluation for more complex defects requires further study.

Acknowledgements

This work was primarily supported by Through-life Engineering Services Centre at Cranfield University. This work was also supported by the UK EPSRC Platform Grant: Through-life performance: From science to instrumentation (Grant number EP/P027121/1).

Conflict of Interest

Authors declare that there are no known conflicts of interest.

References

[1] P. Cotic, D. Kolaric, V.B. Bosiljkov, V. Bosiljkov, Z. Jaglicic, Determination of the applicability and limits of void and delamination detection in concrete structures using infrared thermography, NDT E Int. 74 (2015) 87–93.
[2] D.S.P. Rao, Infrared thermography and its applications in civil engineering, Indian Concr. J. 82 (5) (2008) 41–50.
[3] W. Wild, Application of infrared thermography in civil engineering, Proc. Est. Acad. Sci. Eng. 13 (4) (2007) 436–444.
[4] I.F. García-tejero, A. Hernández, C.M. Padilla-díaz, A. Diaz-espejo, J.E. Fernández, Assessing plant water status in a hedgerow olive orchard from thermography at plant level, Agric. Water Manage. 188 (2017) 50–60.
[5] I. Grubišić, L. Gjenero, T. Lipić, I. Sović, T. Skala, Medical 3D thermography system, Period. Biol. 113 (4) (2011) 401–406.
[6] B.B. Lahiri, S. Bagavathiappan, T. Jayakumar, J. Philip, Medical applications of infrared thermography: a review, Infrared Phys. Technol. 55 (4) (2012) 221–235.

[7] W.H. Maes, A. Baert, A.R. Huete, P.E.H. Minchin, W.P. Snelgar, K. Steppe, A new wet reference target method for continuous infrared thermography of vegetations, Agric. For. Meteorol. 226–227 (2016) 119–131.
[8] D.D. Soerensen, S. Clausen, J.B. Mercer, L.J. Pedersen, Determining the emissivity of pig skin for accurate infrared thermography, Comput. Electron. Agric. 109 (2014) 52–58.
[9] A. Szentkuti, H.S. Kavanagh, S. Grazio, Infrared thermography and image analysis for biomedical use, Period. Biol. 113 (4) (2011) 385–392.
[10] C. Laforte, M.M. Tremblay, Cold regions science and technology comparative evaluation of the anti-icing protection time of runway deicers using infrared thermography, Cold Reg. Sci. Technol. 138 (2017) 57–62.
[11] C. Meola, G.M. Carlomagno, A. Squillace, A. Vitiello, Non-destructive evaluation of aerospace materials with lock-in thermography, Eng. Fail. Anal., vol. 13, no. 3 SPEC. ISS., 2006, pp. 380–388.
[12] B. Yang, Y. Huang, L. Cheng, Defect detection and evaluation of ultrasonic infrared thermography for aerospace CFRP composites, Infrared Phys. Technol. 60 (2013) 166–173.
[13] C. Ibarra-Castanedo, M. Genest, P. Servais, X.P.V. Maldague, A. Bendada, Qualitative and quantitative assessment of aerospace structures by pulsed thermography, Nondestruct. Test. Eval. 22 (2007) 199–215.
[14] N.P. Avdelidis, D.P. Almond, A. Dobbinson, B.C. Hawtin, C. Ibarra-Castanedo, X. Maldague, Aircraft composites assessment by means of transient thermal NDT, Prog. Aerosp. Sci. 40 (3) (2004) 143–162.
[15] S. Shepard, Flash thermography of aerospace composites, in: IV Conf. Panam. END Buenos Aires, 2007, p. 7.
[16] A. D'Annibale, A. Di Ilio, M. Trozzi, L. Bonaventura, The use of infrared thermography for maintenance purposes in the production process of components for automotive alternators, in: Procedia CIRP, vol. 38, 2015, pp. 143–146.
[17] Z. Xu, H. Zhang, Z. Yan, F. Liu, P.K. Liaw, W. Wang, Three-point-bending fatigue behavior of AZ31B magnesium alloy based on infrared thermography technology, Int. J. Fatigue 95 (2017) 156–157.
[18] R.D. Adams, P. Cawley, Defect types and non-destructive testing techniques for composites and bonded joints, Constr. Build. Mater. 3 (4) (1989) 170–183.
[19] X.P. Ding, H.M. Li, J.Q. Zhu, G.Y. Wang, H.Z. Cao, Q. Zhang, H.L. Ma, Application of infrared thermography for laser metal-wire additive manufacturing in vacuum, Infrared Phys. Technol. 81 (2017) 166–169.
[20] D. Yang, G. Wang, G. Zhang, Thermal analysis for single-pass multi-layer GMAW based additive manufacturing using infrared thermography, J. Mater. Process. Technol. 244 (2017) 215–224.
[21] J. Yang, S. Hwang, Y.K. An, K. Lee, H. Sohn, Multi-spot laser lock-in thermography for real-time imaging of cracks in semiconductor chips during a manufacturing process, J. Mater. Process. Technol. 229 (2016) 94–101.
[22] Y. Zhao, L. Tinsley, S. Addepalli, J. Mehnen, R. Roy, A coefficient clustering analysis for damage assessment of composites based on pulsed thermographic inspection, NDT E Int. 44 (Jun. 2016) 59–67.
[23] Y. Zhao, J. Mehnen, W. Xu, M. Alrashed, S. Abineri, R. Roy, Degradation assessment of industrial composites using thermography, in: Procedia CIRP, vol. 38, 2015, pp. 147–152.
[24] D.P. Almond, S.K. Lau, Defect sizing by transient thermography. I. An analytical treatment, J. Phys. D-Appl. Phys. 27 (1994) 1063–1069.
[25] M.B. Saintey, D.P. Almond, Defect sizing by transient thermography. II. A numerical treatment, J. Phys. D. Appl. Phys. 28 (12) (1995) 2539–2546.
[26] J.G. Sun, Analysis of pulsed thermography methods for defect depth prediction, J. Heat Transfer 128 (4) (2006) 329.
[27] P.H. Vahid, S. Hesabi, X. Maldague, The effect of pre-processing techniques in detecting defects of thermal images, in: Proceedings of the VIIth International Workshop on Advances in Signal Processing for Non Destructive Evaluation of Materials, 2013, pp. 53–54.
[28] W.Y. Jeong, C.J. Earls, W.D. Philpot, A.T. Zehnder, Inverse thermographic characterization of optically unresolvable through cracks in thin metal plates, Mech. Syst. Signal Process. 27 (Feb.) (2012) 634–650.
[29] K. Philipp, A. Filippatos, R. Kuschmierz, A. Langkamp, M. Gude, A. Fischer, J. Czarske, Multi-sensor system for in situ shape monitoring and damage identification of high-speed composite rotors, Mech. Syst. Signal Process. 76–77 (Aug.) (2016) 187–200.
[30] C.J. Earls, Stochastic inverse thermographic characterization of sub-pixel sized through cracks, Mech. Syst. Signal Process. 30 (Jul.) (2012) 146–156.
[31] X. Maldague, S. Marinetti, Pulse phase infrared thermography, J. Appl. Phys. 79 (5) (1996) 2694.
[32] C. Ibarra-Castanedo, Quantitative subsurface defect evaluation by pulsed phase thermography: depth retrieval with the phase, University of Laval, 2005.
[33] C. Ibarra-Castanedo, X.P. V. Maldague, Defect depth retrieval from pulsed phase thermographic data on plexiglas and aluminum samples, in: Proc. SPIE, Thermosense XXVI, vol. 5405, 2004, pp. 348–356.
[34] X.P.V. Maldague, Theory and Practice of Infrared Technology for Nondestructive Testing, Wiley, New York, 2001.
[35] X. Han, L.D. Favro, P.K. Kuo, R.L. Thomas, Early-time pulse-echo thermal wave imaging, in: Review of Progress in Quantitative Nondestructive Evaluation, Springer US, Boston, MA, 1996, pp. 519–524.
[36] L.D. Favro, H.J. Jin, Y.X. Wang, T. Ahmed, X. Wang, P.K. Kuo, R.L. Thomas, IR thermal wave tomographic studies of structural composites, in: Review of Progress in Quantitative Nondestructive Evaluation, Springer US, Boston, MA, 1992, pp. 447–451.
[37] L.D. Favro, X. Han, Y. Wang, P.K. Kuo, R.L. Thomas, Pulse-echo thermal wave imaging, in: Review of Progress in Quantitative Nondestructive Evaluation, vol. 14, no. 1, Springer US, Boston, MA, 1995, pp. 425–429.
[38] L.D. Favro, X. Han, P.K. Kuo, R.L. Thomas, Imaging the early time behavior of reflected thermal wave pulses, in: Proceedings of SPIE, Thermosense XVII, vol. 2473, 1995, pp. 162–166.
[39] Z. Zeng, C. Li, N. Tao, L. Feng, C. Zhang, Depth prediction of non-air interface defect using pulsed thermography, NDT E Int. 48 (2012) 39–45.
[40] H.I. Ringermacher, R.J. Archacki, W.A. Veronesi, Nondestructive testing: transient depth thermography, US Patent 5,711,603, 1998.
[41] M. Pilla, M. Klein, X. Maldague, A. Salerno, New absolute contrast for pulsed thermography, in: Proceedings of the 2002 International Conference on Quantitative InfraRed Thermography, vol. 1, no. 1, 2002, pp. 53–58.
[42] S.M. Shepard, J.R. Lhota, B.a. Rubadeux, D. Wang, T. Ahmed, Reconstruction and enhancement of active thermographic image sequences, Opt. Eng. 42 (5) (2003) 1337–1342.
[43] Z. Zeng, J. Zhou, N. Tao, L. Feng, C. Zhang, Absolute peak slope time based thickness measurement using pulsed thermography, Infrared Phys. Technol. 55 (2–3) (2012) 200–204.
[44] J.G. Sun, Method for determining defect depth using thermal imaging, US 6,542,849 B2, 2003.
[45] Y. Zhao, J. Mehnen, A. Sirikham, R. Roy, A novel defect depth measurement method based on Nonlinear System Identification for pulsed thermographic inspection, Mech. Syst. Signal Process. 85 (Feb.) (2017) 382–395.
[46] D. Palumbo, U. Galietti, Damage Investigation in composite materials by means of new thermal data processing procedures, Strain 52 (4) (2016) 276–285.
[47] F. Lopez, C. Ibarra-Castanedo, V. de Paulo Nicolau, X. Maldague, Optimization of pulsed thermography inspection by partial least-squares regression, NDT E Int. 66 (Sep.) (2014) 128–138.
[48] S.K. Lau, D.P. Almond, J.M. Milne, A quantitative analysis of pulsed video thermography, NDT E Int. 24 (4) (1991) 195–202.
[49] C. Ibarra-Castanedo, J.-M. Piau, S. Guilbert, N.P. Avdelidis, M. Genest, A. Bendada, X.P.V. Maldague, Comparative study of active thermography techniques for the nondestructive evaluation of honeycomb structures, Res. Nondestruct. Eval. 20 (1) (2009) 1–31.
[50] W. Minkina, S. Dudzik, Errors of measurements in infrared thermography, in: Infrared Thermography, John Wiley & Sons Ltd, Chichester, UK, 2009, pp. 61–80.